



Effect of processing conditions on the mechanical properties of bio-inspired mechanical gradient nanocomposites

Yefei Zhang^{a,b}, Alexandra N. Edelbrock^c, Stuart J. Rowan^{a,b,d,e,*}

^a Institute for Molecular Engineering, University of Chicago, 5640 S Ellis Ave., Chicago, IL 60637, United States

^b Department of Macromolecular Science and Engineering, Case Western Reserve University, 2100 Adelbert Rd, Cleveland, OH 44106, United States

^c Department of Biomedical Engineering, Case Western Reserve University, 10900 Euclid Ave, Cleveland, OH 44106, United States

^d Department of Chemistry, University of Chicago, 5735 S Ellis Ave., Chicago, IL 60637, United States

^e Chemical and Engineering Sciences, Argonne National Laboratory, 9700 Cass Ave, Lemont, IL 60439, United States

ARTICLE INFO

Keywords:

Bioinspiration
Nanocomposites
Mechanical gradient
Cellulose nanocrystals

ABSTRACT

Photo-induced thiol-ene crosslinking of allyl-functionalized cellulose nanocrystal (CNC)/polymer nanocomposites allows access to films that mimic the water-enhanced mechanical gradient characteristics of the squid beak. These films are prepared by mixing the functionalized CNCs and polymer in a solvent before solution casting and drying. The photocrosslinking agents are then imbibed into the film before UV exposure. Reported herein are studies aimed at better understanding the effect of the film preparation procedure, film thickness and the conditions under which the UV treatment is carried out. It was found that when the film is heated at a temperature higher than its glass transition temperature (T_g) during the UV irradiation step there is a greater enhancement in the mechanical properties of the films, presumably on account of more efficient crosslinking between the CNC fillers. Moreover, composite films that were compression molded (at 90 °C) before the imbibing step displayed lower mechanical properties compared to the as-cast films, which is attributed to phase separation of the CNC fillers and polymer matrix during this additional processing step. Finally, the film thickness was also found to be a critical factor that affects the degree of crosslinking. For example, thinner films (50 μm) displayed a higher wet modulus ca. 130 MPa compared to ca. 80 MPa for the thicker films (150 μm). Understanding the processing conditions allows access to a larger range of mechanical properties which is important for the design of new bio-inspired mechanical gradient nanocomposites.

1. Introduction

The rapid development of modern technologies continues to push the demands for materials with improved properties and functionalities. When designing and fabricating high-performance synthetic materials, nature provides ample inspiration [1–5] and natural materials often demonstrate remarkable properties which distinguish them from their synthetic counterparts [6]. To obtain such properties, biological systems have optimized their complex hierarchical structures over multiple length scales [7–10]. One use of these hierarchical structures is to connect materials with different mechanical properties [11–14]. A squid's beak is an ideal example of how nature seamlessly bridges between the stiff tip of the beak (rostrum) and the soft foundation tissue (buccal) that spans 2 orders of magnitude in stiffness [15–17]. Squid beaks are composed of chitin fibers, water and matrix proteins that are chemically crosslinked, where both the relative concentration of each component as well as the degree of crosslinking varies spatially [17]. It

is proposed that the hydrophobic, histidine-rich proteins (DgHBPs) form coacervate solutions that diffuse into the chitin-binding protein (DgCBPs) scaffold and induce crosslinking between histidine residues with both 4-methylcatechol and peptidyl catechol moieties (L-DOPA). Near the rostrum, a higher fraction of protein is found with a high crosslink density resulting in high stiffness and less hydration (~15 wt %). Inversely, the buccal region of the beak contains a lower amount of protein and fewer crosslinks yielding a softer material with significantly more water (~70 wt%). In dehydrated samples, the difference in modulus between the rostrum and buccal regions is only a factor of 2 times (5–10 GPa), indicating that water swelling is critical in defining the mechanical gradient of the squid beak. When hydrated, the chitin-rich soft base swells significantly, while the rostrum's highly-crosslinked network saturated with hydrophobic and H-bonding catechol moieties prevents significant swelling. This produces an impressive mechanical gradient with a two order of magnitude increase in stiffness across the beak.

* Corresponding author.

E-mail address: stuartrowan@uchicago.edu (S.J. Rowan, >,).

<https://doi.org/10.1016/j.eurpolymj.2019.03.022>

Received 21 November 2018; Received in revised form 6 March 2019; Accepted 8 March 2019

Available online 09 March 2019

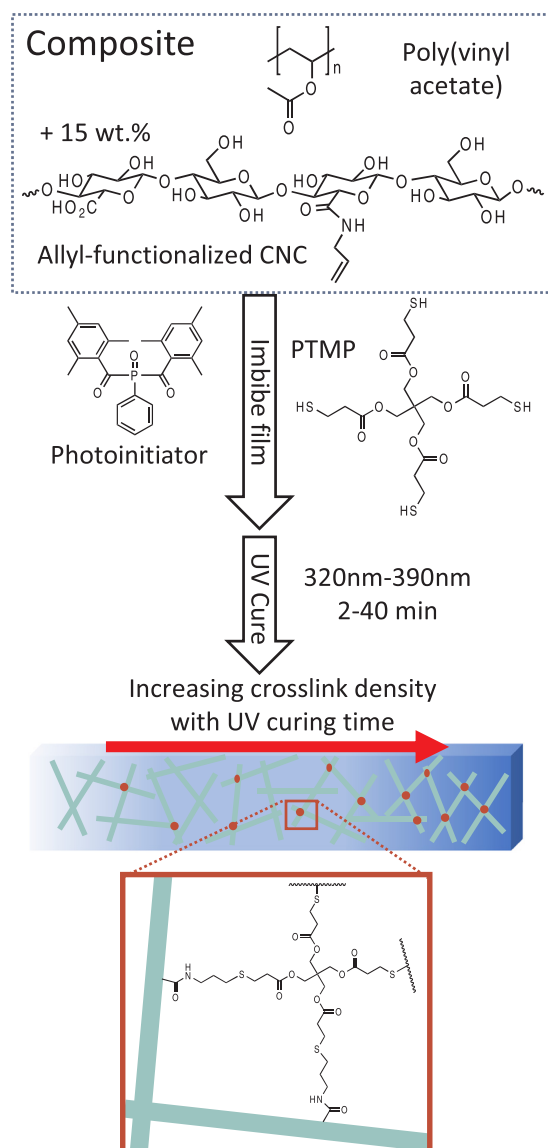
0014-3057/ © 2019 Elsevier Ltd. All rights reserved.

Adoption of nature's gradient strategies offers new and interesting ways to design synthetic mechanical gradient materials [2]. These materials can be used as a modulus buffer where stiff therapeutic implant devices are in immediate contact with soft biological tissues, such as glucose sensors for diabetics [18], osseointegrated prosthetic limbs for amputees [19], long term intravascular interfaces [20], as well as biocompatible intracortical microelectrodes [21–23]. There are a few prior studies published on bioinspired mechanical gradient materials. For example, previous reported approaches to lateral gradient materials have controlled the relative concentration of the stiff and soft components, e.g. with different PDMS elastomers [24] or cellulose nanofibrils/polymer mixtures, along the lateral direction of the films [25]. Alternatively, controlling the degree of alignment of carbon nanotubes (CNT), from well-aligned to random, along the films [26] also yields gradient materials. Finally, more akin the squid beak mechanism, gradient films have been developed by varying degree of crosslinking along the film e.g. using catechol-functionalized chitosan with iron oxide nanoparticles [27], chitosan fillers with L-dopa [28], or imidazole-containing polymers with metals ions [29]. Although these synthetic materials all showed contrast in mechanical stiffness, they lack facile control of a continuous transition in stiffness, suffer from a small range of mechanical contrast, and/or required special equipment or time-consuming steps to access.

In prior work, Rowan and Weder have developed mechanically dynamic polymer nanocomposites which were inspired by the stimuli-responsive behavior of the inner dermis of the sea cucumber [30]. By embedding cellulose nanocrystals (CNCs) in different polymer matrices, a series of polymer nanocomposites that exhibit water-responsive mechanically adaptable behavior were accessed [31–36]. CNCs are highly crystalline nanofibers, which are approximately 5 to 25 nm in cross-section, and hundreds of nanometers to microns in length, depending on the biosource that they are isolated from [37–41]. It has been proposed that when processed correctly CNCs can form a percolating network within the polymer matrix through strong hydrogen bonding interactions [42], which results in a significant enhancement of the mechanical properties of dry composites. Immersion of these nanocomposites into water allows the materials to switch from stiff to soft, on account of the disengagement of the CNC network (and presumably also reduction of CNC-matrix interactions, depending on the nature of the matrix) via competitive hydrogen bonding between the CNCs and water molecules. Another attractive feature of CNCs is that their surface properties can be tailored for different applications by functionalization of the surface hydroxyl groups [43–58].

Inspired by the squid beak model, previous studies have shown that selective photo-irradiation of an allyl-functionalized CNC/polymer (Poly(vinyl acetate), PVAc) nanocomposite film imbided with a tetra-thiol crosslinker (pentaerythritol tetrakis(3-mercaptopropionate), PTMP) and photoinitiator allow access to water-enhanced mechanical gradient materials (Scheme 1) [59]. By introducing crosslinkable functionalities onto the surface of the CNC nanofillers, the original hydrogen bonding interactions can be augmented with covalent crosslinks. The CNC-CNC interactions would then be permanently “switched on” and thus the degree of mechanical softening of the composite materials upon exposure to water could be greatly reduced. As a result of the formation of a permanent covalent CNC crosslinked network access to films with a wet modulus of over 100 MPa can be achieved, relative to ca. 30 MPa for composites that only use the noncovalent interactions that are disrupted by the presence of water. Furthermore, by utilizing UV-initiated thiol-ene chemistry it was shown that the degree of swelling and the magnitude of the wet modulus (presumably by controlling the amount of crosslinking) could be controlled by irradiation time.

Though polymer nanocomposites with a water-activated mechanical gradient have been successfully achieved, the level of mechanical contrast (E_{stiff}/E_{soft} ca. 5) is still relatively low compared to the mechanical gradient of the squid beak, which ranges from ca. 50 MPa to



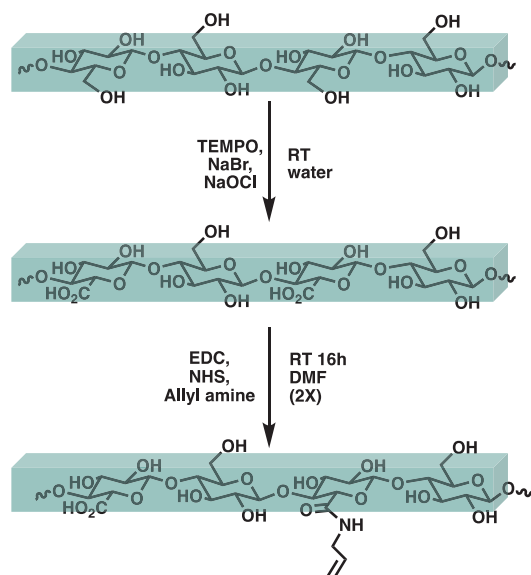
Scheme 1. Schematic of the procedure used to access the squid beak mimetic composites and the proposed photo-initiated thiol-ene crosslinking reaction of the CNC nanofillers.

5 GPa. Furthermore, during studies following this initial work, it was found that the final wet modulus of the films was very sensitive to a number of processing and film factors which lead to inconsistent results. Specifically, this includes the temperature of the film and the nature of the supporting substrate during the UV curing step, as well as the how the uncured films are processed and their resulting thickness. The work reported herein was aimed at investigating some of these aspects in more detail with the goal of producing a more robust protocol.

2. Experimental section

2.1. Materials

Cellulose nanocrystals were isolated from sea tunicates (*Styela Clava*) that were harvested from floating docks in Warwick Marina (Warwick, RI) and were cleaned and bleached following previously published procedures [34]. NaOCl was received from Alfa Aesar with 14.5% available chlorine. Poly(vinyl acetate) (PVAc) with weight-average molecular weight, $M_w = 100\,000$ g/mol, and all the other



Scheme 2. Chemistry used to access the allyl-functionalized CNCs.

reagents were purchased from Sigma-Aldrich and used as received.

2.2. Synthesis of tCNC-COOH via TEMPO oxidation

Dry, bleached tunicate mantles were hydrolyzed using hydrochloric acid and then oxidized using TEMPO, NaBr and NaOCl to yield tCNC-COOH according to literature procedures [60]. The tCNC-COOHs were titrated using conductometric titration in order to determine the amount of surface carboxylic groups. Briefly, 25 mg of tCNC-COOH was dispersed in 80 mL of DI water by sonication overnight in a Branson CPX sonication bath. 15 μ L of concentrated HCl (33 wt%) was added under stirring to drop the pH of the dispersion below 3 and the titration was performed using 0.01 M NaOH solution. The conductivity was plotted against the volume of NaOH consumed and the plateau region was used to determine the carboxylic acid group content.

2.3. Synthesis of allyl-functionalized CNCs (tCNC-allyl-COOH)

Allyl functionalization was performed using similar EDC and NHS peptide coupling methods used previously [50] with slight modifications (Scheme 2). Oxidized CNCs (200 mg, 0.2 mmol of carboxylic acid moieties) were dispersed in 40 mL of DMF and bath sonicated overnight. 1-Ethyl-3-(3-(dimethylamino)propyl) carbodiimide hydrochloride (EDC) (383.4 mg, 2 mmol, 10 equiv.) was added to the dispersion and the reaction was stirred for 5 min. Then *N*-hydroxysuccinimide (NHS) (230.2 mg, 2 mmol, 10 equiv.) was added and stirred for a further 30 min. Finally, allylamine (228.4 mg, 4 mmol, 20 equiv.) was slowly added and the reaction was allowed to stir for 16 hrs at room temperature. The resulting mixture was precipitated in excess methanol and then centrifuged at 10 000 rpm for 10 min. The residual was washed with methanol (3X) and DI water (3X) under successive centrifugation. Functionalized CNCs were re-dispersed in DI water, dialyzed and lyophilized to yield tCNC-allyl-COOH. This allyl functionalization was repeated again under the same conditions to enhance the degree of functionalization. The final product was titrated again to determine the residual amount of carboxylic acid groups, and the amount of allyl groups was calculated by the difference in the number of carboxylic acids groups before and after the reaction

2.4. Characterization of tCNC-COOH and tCNC-allyl-COOH

Atomic Force Microscopy (AFM). The dimensions of tCNC-COOHs

and tCNC-allyl-COOHs were measured by AFM. Aqueous suspensions of tCNC-COOHs and tCNC-allyl-COOHs with a concentration of 0.1 mg/mL were drop cast on freshly cleaved mica surface. The samples were imaged in scan assist mode using a Bruker Multimode 8 instrument equipped with a Nanoscope 5 controller. The length and thickness of the CNCs were analyzed using the height image by Gwyddion software.

X-ray Diffraction (XRD). The degree of crystallinity before and after allyl-functionalization was measured by XRD. Lyophilized samples were tightly packed inside plastic washers and were held in place between two pieces of Kapton tape. The XRD patterns were recorded using a SAXSLAB GANESHA 300 XL system with Cu K α source ($\lambda = 0.154$ nm) at a voltage of 40 kV and 40 mA power. The crystallinity index (C.I.) was calculated according to the following equation:

$$C. I. = \frac{I_{200} - I_{AM}}{I_{200}} \times 100\% \quad (1)$$

where I_{200} is the intensity of the (2 0 0) reflection and I_{AM} is the intensity at $2\theta = 18^\circ$, corresponding to the minimum between the planes (2 0 0) and (1 1 0).

X-ray Photoelectron Spectroscopy (XPS). The XPS data were collected using the AXIS Nova spectrometer equipped with a monochromatic Al K α X-ray source. The Al anode was powered at 10 mA and 15 kV. Instrument base pressure was ca. 1×10^{-10} Torr. For calibration purposes, the binding energies were referenced to C-C/C-H peak in the C 1s signal at 285.0 eV. Lyophilized tCNC-COOH and tCNC-allyl-COOH samples were pressed into pellets and adhered to conductive carbon tape before loading into the instrument.

Elemental Analysis. tCNC-COOH and tCNC-allyl-COOH were washed with 0.1 M HCl to protonate all the carboxylic groups. The samples were then lyophilized, and the carbon, hydrogen and nitrogen contents were measured at Midwest Microlab (Indianapolis, Indiana, USA).

2.5. Fabrication of CNC/PVAc nanocomposites

PVAc was dissolved in DMF (50 mg/mL) by stirring for 4 hrs, while tCNC-allyl-COOH was homogeneously dispersed in DMF (3 mg/mL) by ultrasonication. The nanocomposite mixture was prepared by mixing appropriate amounts of the PVAc solution and CNC dispersion and ultrasonicated for 30 min before casting into PTFE dishes. The samples were heated at 60 $^\circ$ C in a vacuum oven for 5 days to fully remove the DMF. The amount of CNC in the final nanocomposites was set at 15 wt % in this study. Thermogravimetric analysis (TGA) was used to confirm the removal of DMF. The dried nanocomposite films were removed from the PTFE dishes and either used as-cast or were compression molded at 90 $^\circ$ C at 4000 psi for 10 min to yield 150 μ m thick films. In the case of the as-cast films, the thickness was controlled by adjusting the amount of CNC/PVAc solutions that were cast into the PTFE dish (diameter 10 cm).

2.6. Imbibing process

The imbibing procedures were adapted from previously published methods with minor modification [59]. CNC/PVAc nanocomposites were cut into rectangular strips with an approximate dimension of 30 mm by 4 mm. Stock solutions of the photoinitiator (Phenylbis(2,4,6-trimethylbenzoyl)phosphine oxide) (2 mM) and crosslinker (pentaerythritol tetrakis(3-mercaptopropionate), PTMP) (10 mM) were prepared by dissolving the reagents in DCM. Then each strip was weighed individually to calculate the amount of allyl groups within the strip based on weight fraction of CNCs and the amount of allyl functionalities on the CNC surface. The required amount of stock solution of photoinitiator (5 mol% of allyl groups) and crosslinker (25 mol% of allyl groups) were mixed. The imbibing was performed by slowly pipetting the initiator and crosslinker co-solution onto the composite strips until the solution was absorbed. The imbibed films were then placed on PTFE dishes and annealed in a desiccator filled with saturated DCM vapor for

24 hrs in a dark environment. The goal of the solvent annealing step is to ensure a more homogeneous distribution of the photoinitiator and crosslinker within the film. Finally, the strips were dried under reduced pressure at room temperature for 24 hrs to remove any residual DCM. TGA was used to confirm the complete removal of DCM.

2.7. Photo-crosslinking procedure

The nanocomposite films were irradiated with a 320–390 nm UV light using a Honle Bluepoint UV source at an intensity of 60 mW/cm² for different times ranging from 2 to 40 min. During the irradiation procedure the films were supported on different substrates, including an aluminum block, foam block or hot plate. All films were turned over at the midpoint of the exposure time to make sure both sides were exposed with the same amount of UV light. All the films were subsequently soaked in 2-propanol for 2 hrs after irradiation to remove any unreacted crosslinkers. This washing step was repeated twice with fresh 2-propanol before the films were dried in vacuum oven for 24 hrs at room temperature and 48 hrs at 40 °C, respectively.

2.8. Water swelling of nanocomposites

All films were first weighed to obtain the dry mass after removal from the oven. The films were then placed in vials filled with DI water, and the vials were placed in a temperature-controlled water bath at 37 °C. After 18 hrs the films were removed, gently blotted using filter paper and weighed to obtain the wet mass. The degree of swelling was calculated by:

$$\%Swelling = \frac{Wet\ mass - Dry\ mass}{Dry\ mass} \times 100 \quad (2)$$

2.9. Dynamic mechanical analysis (DMA) characterization of nanocomposites

The viscoelastic properties of nanocomposites were analyzed using a RSA-G2 solid analyzer (TA Instrument, DE) equipped with a tension clamp and submersion chamber allowing the measurements to be conducted while the films were immersed in water. The wet modulus of the samples was analyzed using a temperature sweep method from 18 °C to 45 °C at a heating rate of 3 °C /min, with a fixed frequency of 1 Hz and a strain of 0.1%. For characterizing the dry modulus of composite films, only the tension camp was used and the same test procedure was used except for the temperature, which was varied from 0 °C to 90 °C. All the tests were performed in triplicate and the standard deviations were plotted as error bars.

3. Results and discussion

3.1. Fabrication of bio-inspired nanocomposites with allyl-functionalized CNCs

To access allyl-functionalized CNCs, CNCs were first isolated from tunicate mantles using hydrochloric acid hydrolysis. TEMPO mediated oxidation was subsequently performed to oxidize some of the primary OH groups into carboxylic acid moieties. Conductometric titrations of these oxidized CNCs show a carboxylic acid density of 1000 mmol/kg (tCNC-COOH₁₀₀₀, where the subscript is the functional group density in mmol/kg). The tCNC-COOH₁₀₀₀ were then functionalized with allylamine using standard peptide coupling chemistry (Scheme 2). The functionalized CNCs showed a residual carboxylic acid density of 200 mmol/kg as measured by conductometric titration, suggesting that 800 mmol/kg of the carboxylic acid groups were functionalized with allylamine (tCNC-allyl₈₀₀-COOH₂₀₀). FTIR studies of tCNC-COOH₁₀₀₀ show a characteristic peak at 1600 cm⁻¹ which is associated with the carboxylate moieties. The formation of the amide bond in tCNC-

allyl₈₀₀-COOH₂₀₀ is confirmed by the appearance of a new carbonyl peak at 1650 cm⁻¹, while the peak at 1600 cm⁻¹ is associated with the residual carboxylate moieties (Fig. S1). Further verification of the functionalization of the CNCs was obtained by XPS and elemental analysis. XPS spectra of the tCNC-allyl₈₀₀-COOH₂₀₀ sample (Fig. S2a) shows a signal corresponding to nitrogen (N 1s: 402 eV). Furthermore, after fitting the high-resolution XPS spectra of the C 1s signal using the peak positions reported by Lin and Dufresne that utilized the same EDC-NHS chemistry [61], a characteristic C-N (286.2 eV) peak is present in the tCNC-allyl₈₀₀-COOH₂₀₀ sample but not in the tCNC-COOH₁₀₀₀ starting material (Fig. S2b and c). Taken together with the elemental analysis results (Table S1 in supporting information), which shows a nitrogen content of 0.6% for tCNC-allyl₈₀₀-COOH₂₀₀, the data is consistent with the successful reaction of allylamine onto the surface of CNCs. The average dimensions of the crystals before and after functionalization were measured using AFM height images (Fig. S3). The tCNC-COOH₁₀₀₀s were found to have an average length of 1186 ± 643 nm and height of 10.2 ± 2.4 nm. The tCNC-allyl₈₀₀-COOH₂₀₀s showed similar dimensions (length 985 ± 454 nm and height 10.3 ± 1.9 nm) confirming that the functionalization did not significantly impact the size of the CNCs and that the tCNC-allyl₈₀₀-COOH₂₀₀s maintained an aspect ratio of ca. 100. The changes in crystallinity before and after allyl-functionalization were measured by XRD (Fig S4). The crystallinity index (C.I.) only changes slightly, from ca. 95.5% to 94% for tCNC-COOH₁₀₀₀ and tCNC-allyl₈₀₀-COOH₂₀₀ respectively, confirming the integrity of the cellulose nanocrystals after functionalization.

In the prior studies the effect of irradiation time and the amount of allyl-functionalized CNCs embedded in a poly(vinyl acetate) (PVAc) matrix on the mechanical properties of these photo-crosslinkable nanocomposites was studied [59]. In this work, PVAc nanocomposites containing 15 wt% of tCNC-allyl-COOH were prepared in order to study the effect that UV irradiation curing conditions, film processing conditions, as well as film thickness, have on the mechanical properties of the crosslinked composite films. All nanocomposites were fabricated by mixing an appropriate amount of a tCNC-allyl₈₀₀-COOH₂₀₀ dispersion in DMF and a PVAc DMF solution followed by casting and drying in a vacuum oven.

3.2. Effect of UV irradiation conditions

In order to more precisely control the thickness of the films the dried composites were first compression molded (at 90 °C) into a smooth and clear film with thickness around 150 μm, and then imbibed with the photoinitiator and the pentaerythritol tetrakis(3-mercaptopropionate) (PTMP) crosslinker at a 20:20:1 M ratio of alkene:thiol:initiator. The films were then irradiated with UV light (intensity 60 mW/cm²) for different times ranging from 2 to 40 mins in order to initiate the thiol-ene reaction. It is important to note that the relatively high-intensity UV source can generate heat during the UV irradiation step. Given that the dry composite films have a T_g at ca. 50 °C, as can be seen from the peak of tan δ on the DMA curves (Fig. S5), it is reasonable to expect that such heating may have an effect on the amount of curing. Thus, initial studies focused on reducing the effect of the UV light induced heat by supporting the composite film on an aluminum block which acts as a heat sink to aid dissipation of any heat generated by the UV light. Films were irradiated for varying time periods up to 40 min (20 min each side). After washing with 2-propanol to remove any residual crosslinker/photoinitiator and drying in a vacuum oven, all films were immersed in water and mechanical testing was conducted on the water swollen films (wet state) after they reached equilibrium swelling. Fig. 1a shows the temperature dependency of the storage modulus (E') of the nanocomposites films as measured by DMA temperature sweep studies. The wet storage modulus (E') shows a transition at ca. 22 °C for all samples which is attributed to the glass transition temperature (T_g) of the PVAc matrix. It should be noted that the T_g of dry PVAc polymer

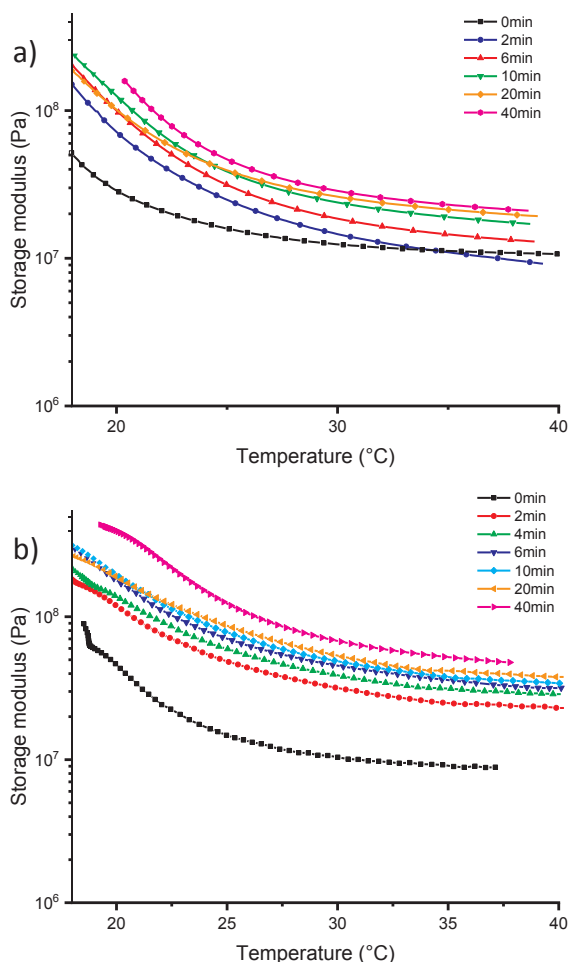


Fig. 1. Representative DMA temperature sweeps of wet 15 wt% tCNC-allyl₈₀₀-COOH₂₀₀/PVAc nanocomposites irradiated on (a) aluminum block (heat sink) and (b) hotplate set at 60 °C.

is around 50 °C, but in the wet state water acts as a plasticizer decreasing the T_g of the polymer matrix. The storage modulus (E') at a temperature higher than T_g (37 °C) was used to evaluate the wet mechanical properties of the films after different UV exposure times. Data in Fig. 1a shows that the E' increased from 10 MPa for un-irradiated sample to 22 MPa for samples irradiated for 40 min. However, based on the prior work on the 15 wt% tCNC-allyl-COOH/PVAc nanocomposites which showed a wet modulus above 100 MPa, the level of mechanical reinforcement observed in Fig. 1a was relatively low, presumably on account of a limited degree of covalent crosslinking of the CNC fillers.

One possible reason for this observation is that the UV-initiated thiol-ene reaction is too slow in the bulk film at temperatures lower than the T_g of PVAc polymer matrix (50 °C), on account of the reagents being locally trapped in the glassy polymer matrix. To test this hypothesis, a series of UV curing experiments were carried out under three different conditions: (1) the films were supported on a non-thermally conducting substrate (foam block); (2) the films were pre-swollen with water to lower the T_g of the polymer to around room temperature (22 °C) before being irradiated with UV; and (3) the films were placed on a hot plate set to 60 °C. Fig. 2a shows the comparison of wet E' at 37 °C for samples irradiated for 40 min using different conditions. There is no significant difference in the E' (23–25 MPa) of the films supported on either a thermal conducting aluminum substrate or a non-thermal conducting foam substrate, suggesting that under these specific experimental conditions the heat generated by the UV source is not enough to warm up the films to above their T_g . In the case of the water-swollen samples, the temperature at which they are irradiated with UV

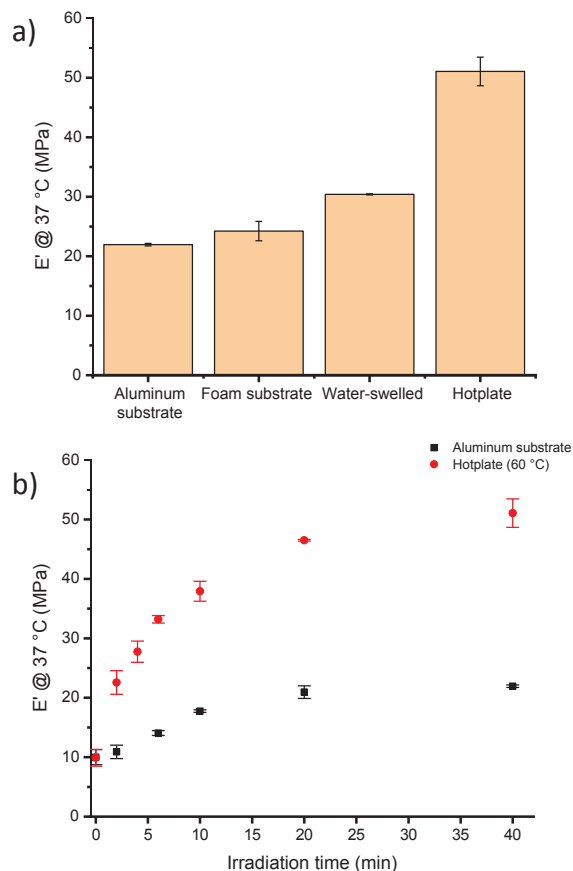


Fig. 2. Comparison of the wet storage modulus (E') at 37 °C of (a) the composite films irradiated for 40 min under different conditions and (b) composite films supported on an aluminum substrate or hotplate (at 60 °C) and irradiated for different times ranging from 2 to 40 min.

light is now very close to the T_g of the polymer matrix, and as a result, the E' of the crosslinked film increases to 30 MPa. However, the biggest increase in mechanical reinforcement was observed for films supported on the hot plate set to a temperature (60 °C) higher than the T_g of the polymer matrix. The wet modulus increased from 10 MPa before irradiation to 50 MPa after irradiating for 40 min (Fig. 1b). This could be explained by the increase in chain mobility facilitating the diffusion of reagents and resulting in a higher level of crosslinking. A comparison of the E' at 37 °C versus irradiation times for films supported on aluminum or on a 60 °C hotplate is shown in Fig. 2b, which clearly shows that the kinetics of the thiol-ene crosslinking reaction had been improved by heating the films above their T_g during UV irradiation. As a result, the mechanical contrast is significantly improved from E'_{stiff}/E'_{soft} ca. 2 to E'_{stiff}/E'_{soft} ca. 5.

3.3. Effect of film processing condition

The above studies used tCNC-allyl-COOH/PVAc nanocomposite films that were compression molded before UV curing. Interestingly, while the films appeared smooth and optically clear after melt processing (Fig. S6), when the films were immersed in water the films appeared slightly inhomogeneous (Fig. S7). It has been shown that melt processing of CNC composites can induce some phase segregation, and this certainly would be expected to have a negative impact on the mechanical reinforcement of the CNC filler [62] as well as the ability of the light to penetrate evenly through the wet film. Thus, a new batch of composite films were prepared and were used as-cast (after the films were dried in the vacuum oven) without any compression molding/melt processing. Upon exposure to water, the as-cast films showed more

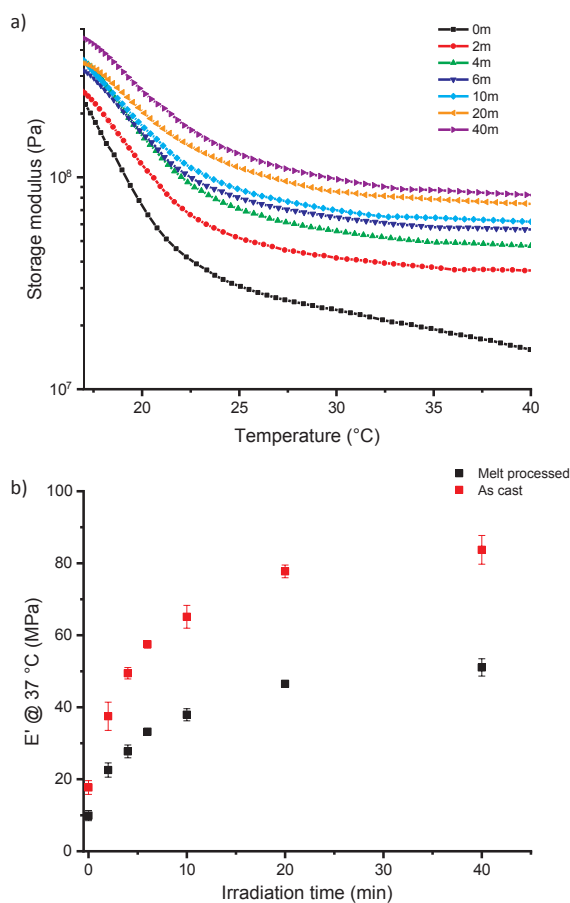


Fig. 3. (a) Representative DMA temperature sweeps of wet as-cast composite films before and after UV irradiation. (b) Comparison of the wet storage modulus (E') of melt-processed films (approximately 150 μm) and as-cast films (approximately 150 μm) at 37 $^{\circ}\text{C}$ plotted against irradiation times.

homogeneous swelling relative to the melt processed films (Fig. S7). Therefore, it is important to study how the different film processing method impacts the mechanical reinforcement of these bio-inspired nanocomposites. It should be noted that the as-cast films should be carefully prepared to ensure they are free of any defects or bubbles, and that the film thickness can be controlled by varying the amount of materials added into the PTFE dish.

As-cast films with a thickness of approximately 150 μm (which matches the thickness of the melt-processed films) were imbibed using the same method as mentioned above. The samples were then placed on a hot plate set at 60 $^{\circ}\text{C}$ and irradiated with UV light at an intensity of 60 mW/cm^2 for times ranging from 2 to 40 mins. As was seen in the prior studies, DMA temperature studies of these films in the wet state (Fig. 3a) confirm that there is an increase in the wet storage modulus (E') upon UV crosslinking. However, these as-cast crosslinked films show a higher magnitude of mechanical reinforcement relative to the melt-processed films (Fig. 3b), suggesting that there is an overall improvement in the degree of covalent crosslinking with the more homogeneous as-cast films. It is also important to point out that the degree of crosslinking could be well-controlled by varying the UV irradiation time resulting in a wet E' ranging between ca. 15 MPa and 80 MPa for the least and most crosslinked sample respectively. As hypothesized above, the inhomogeneity after melt processing should not only disrupt the CNC filler network, but could also limit the amount of UV that can penetrate through the film. One way to test this effect is to measure how the UV intensity changes as it passes through the different films. Results showed that the intensity (preset to 60 mW/cm^2) decreased to $45.2 \pm 0.8 \text{ mW}/\text{cm}^2$ after penetrating through as-cast films,

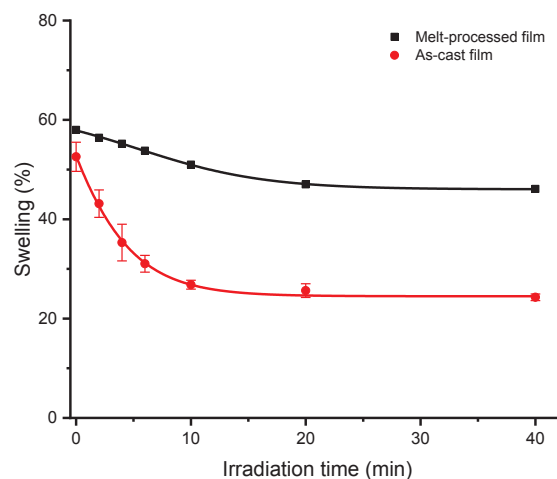


Fig. 4. Equilibrium swelling data versus irradiation time of 150 μm thick melt-processed and as-cast films.

whereas it dropped to $21.3 \pm 0.7 \text{ mW}/\text{cm}^2$ for melt-processed films. Considering both films have similar thickness (approximately 150 μm), the results suggest that the inhomogeneity of melt processed films does indeed block more UV light which, in turn, presumably contributes to a lower degree of crosslinking.

It can be expected that as the degree of crosslinking increases then there should be a decrease in the degree of water swelling. Therefore, the water uptake of both the melt-pressed films and as-cast films after crosslinking were measured, and the equilibrium swelling data versus irradiation time were plotted in Fig. 4. As expected, the degree of swelling decreased from 60% to 24% after exposure of the as-cast films to UV irradiation, which is much lower than the degree of swelling observed in the cured melt-pressed films (50%), further supporting the fact that a higher degree of crosslinking is observed in the as-cast films. The viscoelastic properties of the crosslinked melt-pressed film and as-cast film in the dry state were also studied (Figs. S8 and S9). As expected, unlike the wet films, the storage modulus of the dry films at temperatures higher than T_g of the matrix show only a slight relative increase after covalent crosslinking. Interestingly, comparison of the dry state E' for the as-cast and melt-processed crosslinked films (ca. 730 MPa vs. ca. 520 MPa, respectively) shows that the as-cast film exhibits a higher plateau modulus. Since the dry modulus above the T_g is significantly impacted by the percolating CNC network, this result is also consistent with melt processing resulting in some disruption of the CNC network.

3.4. Effect of film thickness

A key aspect of any photocuring process is the ability of the light to penetrate through the film. In fact, if these films are only irradiated on one side they curl when exposed to water, presumably on account of different degrees of water swelling of the top and bottom surfaces. This can be explained by the limited penetration of the UV light through the composite film resulting in an uneven distribution of crosslinking across the film thickness. The hypothesis is further backed up by measuring the intensity of the UV light that penetrates through the composite films (Fig. 5), which clearly shows a drop in penetrating UV intensity with increasing composite film thickness. It is worthy of note that a similar study on neat PVAc films (without any CNCs) shows little-to-no effect on UV light penetration irrespective of the film thickness studied (intensity only decrease from 60 mW/cm^2 to $58.3 \pm 0.1 \text{ mW}/\text{cm}^2$ going from ca. 50–150 μm). This suggests that the decrease in UV intensity for the as cast composite films can be attributed to the scattering of UV light by the CNCs. As such, even though the above films are irradiated on both sides, the limited UV penetration depth could still lead to an

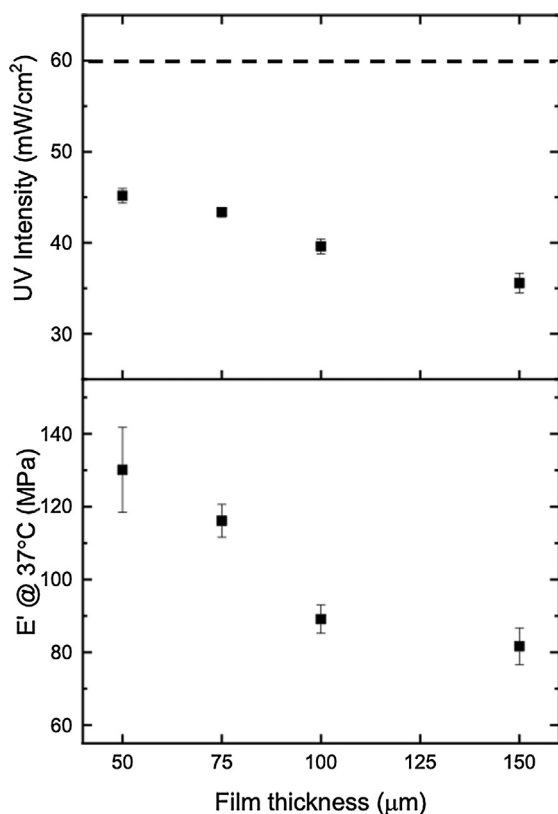


Fig. 5. UV intensity measured after penetrating through as-cast composite films (contain 15 wt% tCNC-allyl-COOH), and a comparison of the wet storage modulus (E') at 37 °C after 40 min UV irradiation versus film thickness. Dash line indicates the original output UV intensity at 60 mW/cm².

uneven distribution of crosslinking between the composite film's surface and center. Such an effect should be more pronounced in thicker films. As the original work was carried out on ca. 60 μm films [59] and the above work focused on much thicker 150 μm films, it is important to understand the effect that film thickness has on the wet mechanical properties of the crosslinked materials.

To this end, composite films with approximate thickness of 50 μm, 75 μm and 100 μm were fabricated and used as-cast. These films were imbibed and crosslinked under the same conditions as the 150 μm films in the above study. All the films were then swollen in water, and their wet state storage modulus after irradiation with UV for 40 mins was measured by DMA. Fig. 5 shows the wet state storage modulus of the films at 37 °C versus film thickness, clearly demonstrating that film thickness does have a significant impact on the wet mechanical properties of these crosslinked films. The wet storage modulus increases from ca. 80 MPa to ca. 130 MPa as the film thickness decreases from 150 μm to 50 μm. This is consistent with the hypothesis that under the same UV irradiation conditions thinner films form a more homogenous covalent crosslinking network through the thickness of the film relative to the thicker films, which in turn results in better overall mechanical properties of the wet films. Even so it is important to note that the 50 μm films are extremely delicate in the wet state making them difficult to handle which was why it was of interest to target the thicker films. The more homogenous networks within thinner films (50 μm) also result in a slight increase in the dry storage modulus (ca. 970 MPa compared with ca. 735 MPa for 150 μm films, Fig. S10). It is also worthwhile pointing out that there is no significant difference in water swelling for these composite films at the different thickness (between 22% and 24%, data not shown here), even though the wet E' show that thinner films have more homogenous crosslinking.

4. Conclusion

Bio-inspired nanocomposites based on allyl-functionalized tunicate CNCs embedded in a PVAc matrix were prepared. The functionalized CNC fillers can be covalently crosslinked using UV initiated thiol-ene chemistry to yield composite films that show tunable mechanical properties upon swelling in water. In order to develop a more reproducible protocol for accessing these films the effects of UV crosslinking conditions, films processing conditions as well as film thickness on the resulting mechanical properties of the films were studied. These conditions were shown to have a significant impact on the final mechanical properties of crosslinked films. The highest level of mechanical reinforcement in the wet state ($E' = 130$ MPa at 37 °C) was achieved by using 50 μm thick as-cast films, which were heated at 60 °C during UV irradiation. In these films a mechanical contrast (E'_{stiff}/E'_{soft}) > 7 of the wet films was observed which is slightly higher than observed in the original work (E'_{stiff}/E'_{soft} ca. 5) [59], indicating how the processing conditions can be used to optimize the wet modulus contrast of these materials. Considerations such as these are beneficial for the development of the next generation of squid beak bio-inspired nanocomposites, potentially allowing access to larger mechanical contrasts that more precisely mimic those observed in the squid beak.

Acknowledgement

This project is supported by the National Science Foundation PIRE program under Grant No. NSF #1743475. Parts of this work were carried out using the Soft Matter Characterization Facility of the University of Chicago. AFM, XRD and XPS were carried out at the Chicago MRSEC center (funded by NSF DMR-1420709). The authors would like to thank Kristen Wek for her help with some experiments and Alexander Filatov for the assistance with the XPS characterization.

Appendix A. Supplementary material

Supplementary data to this article can be found online at <https://doi.org/10.1016/j.eurpolymj.2019.03.022>.

References

- [1] L. Montero de Espinosa, W. Meesorn, D. Moatsou, C. Weder, Bioinspired polymer systems with stimuli-responsive mechanical properties, *Chem. Rev.* 117 (2017) 12851–12892, <https://doi.org/10.1021/acs.chemrev.7b00168>.
- [2] Z. Liu, M.A. Meyers, Z. Zhang, R.O. Ritchie, Functional gradients and heterogeneities in biological materials: design principles, functions, and bioinspired applications, *Prog. Mater. Sci.* 88 (2017) 467–498, <https://doi.org/10.1016/j.pmatsci.2017.04.013>.
- [3] C. Zhang, D.A. Mcadams, J.C. Grunlan, Nano/micro-manufacturing of bioinspired materials: a review of methods to mimic natural structures, *Adv. Mater.* 28 (2016) 6292–6321, <https://doi.org/10.1002/adma.201505555>.
- [4] G. Zan, Q. Wu, Biomimetic and bioinspired synthesis of nanomaterials/nanostructures, *Adv. Mater.* 28 (2016) 2099–2147, <https://doi.org/10.1002/adma.201503215>.
- [5] U.G.K. Wegst, H. Bai, E. Saiz, A.P. Tomsia, R.O. Ritchie, Bioinspired structural materials, *Nat. Mater.* 14 (2015) 23–36, <https://doi.org/10.1038/nmat4089>.
- [6] M.A. Meyers, J. McKittrick, P.-Y. Chen, Structural biological materials: critical mechanics-materials connections, *Science* 339 (2013) 773–779, <https://doi.org/10.1126/science.1220854>.
- [7] P.-Y. Chen, A.Y.M. Lin, Y.-S. Lin, Y. Seki, A.G. Stokes, J. Peyras, E.A. Olevsky, M.A. Meyers, J. McKittrick, Structure and mechanical properties of selected biological materials, *J. Mech. Behav. Biomed. Mater.* 1 (2008) 208–226, <https://doi.org/10.1016/j.jmbbm.2008.02.003>.
- [8] W. Yang, I.H. Chen, B. Gludovatz, E.A. Zimmermann, R.O. Ritchie, M.A. Meyers, Natural flexible dermal armor, *Adv. Mater.* Deerfield Beach Fla. 25 (2013) 31–48, <https://doi.org/10.1002/adma.201202713>.
- [9] R.O. Ritchie, Natural materials: armoured oyster shells, *Nat. Mater.* 13 (2014) 435–437, <https://doi.org/10.1038/nmat3956>.
- [10] P. Vukusic, J.R. Sambles, Photonic structures in biology, *Nature* 424 (2003) 852–855, <https://doi.org/10.1038/nature01941>.
- [11] L. Farren, S. Shayler, A.R. Ennos, The fracture properties and mechanical design of human fingernails, *J. Exp. Biol.* 207 (2004) 735–741, <https://doi.org/10.1242/jeb.00814>.
- [12] M. Benjamin, H. Toumi, J.R. Ralphs, G. Bydder, T.M. Best, S. Milz, Where tendons and ligaments meet bone: attachment sites ('entheses') in relation to exercise and/or mechanical load, *J. Anat.* 208 (2006) 471–490, <https://doi.org/10.1111/j.1469->

- 7580.2006.00540.x.
- [13] H.H. Lu, S. Thomopoulos, Functional attachment of soft tissues to bone: development, healing, and tissue engineering, *Annu. Rev. Biomed. Eng.* 15 (2013) 201–226, <https://doi.org/10.1146/annurev-bioeng-071910-124656>.
- [14] C. Sun, J.H. Waite, Mapping chemical gradients within and along a fibrous structural tissue, *Mussel Byssal Threads*, *J. Biol. Chem.* 280 (2005) 39332–39336, <https://doi.org/10.1074/jbc.M508674200>.
- [15] A. Miserez, Y. Li, J.H. Waite, F. Zok, Jumbo squid beaks: Inspiration for design of robust organic composites, *Acta Biomater.* 3 (2007) 139–149, <https://doi.org/10.1016/j.actbio.2006.09.004>.
- [16] A. Miserez, T. Schnerberk, C. Sun, F.W. Zok, J.H. Waite, The transition from stiff to compliant materials in squid beaks, *Science* 319 (2008) 1816–1819, <https://doi.org/10.1126/science.1154117>.
- [17] Y. Tan, S. Hoon, P.A. Guerette, W. Wei, A. Ghabban, C. Hao, A. Miserez, J.H. Waite, Infiltration of chitin by protein coacervates defines the squid beak mechanical gradient, *Nat. Chem. Biol.* 11 (2015) 488–495, <https://doi.org/10.1038/nchembio.1833>.
- [18] K.L. Helton, B.D. Ratner, N.A. Wisniewski, Biomechanics of the sensor-tissue interface—effects of motion, pressure, and design on sensor performance and the foreign body response—Part I: theoretical framework, *J. Diabetes Sci. Technol.* 5 (2011) 632–646, <https://doi.org/10.1177/193229681100500317>.
- [19] P. Fleckman, J.E. Olerud, Models for the histologic study of the skin interface with percutaneous biomaterials, *Biomater. Mater.* 3 (2008) 034006, <https://doi.org/10.1088/1748-6041/3/3/034006>.
- [20] U.K. Teichgräber, R. Pfitzmann, H.A.F. Hofmann, Central Venous Port Systems as an Integral Part of Chemotherapy, *Dtsch. Aerzteblatt Online* (2011), <https://doi.org/10.3238/arztebl.2011.0147>.
- [21] J.R. Capadona, D.J. Tyler, C.A. Zorman, S.J. Rowan, C. Weder, Mechanically adaptive nanocomposites for neural interfacing, *MRS Bull.* 37 (2012) 581–589, <https://doi.org/10.1557/mrs.2012.97>.
- [22] J.P. Harris, A.E. Hess, S.J. Rowan, C. Weder, C.A. Zorman, D.J. Tyler, J.R. Capadona, *In vivo* deployment of mechanically adaptive nanocomposites for intracortical microelectrodes, *J. Neural Eng.* 8 (2011) 046010, <https://doi.org/10.1088/1741-2560/8/4/046010>.
- [23] M. Jorfi, J.L. Skousen, C. Weder, J.R. Capadona, Progress towards biocompatible intracortical microelectrodes for neural interfacing applications, *J. Neural Eng.* 12 (2015) 011001, <https://doi.org/10.1088/1741-2560/12/1/011001>.
- [24] K.U. Claussen, R. Giesa, T. Scheibel, H.-W. Schmidt, Learning from nature: synthesis and characterization of longitudinal polymer gradient materials inspired by mussel byssus threads, *Macromol. Rapid Commun.* 33 (2012) 206–211, <https://doi.org/10.1002/marc.201100620>.
- [25] B. Wang, A.J. Benitez, F. Lossada, R. Merindol, A. Walther, Bioinspired mechanical gradients in cellulose nanofibril/polymer nanopapers, *Angew. Chem. Int. Ed.* 55 (2016) 5966–5970, <https://doi.org/10.1002/anie.201511512>.
- [26] Z. Lin, X. Gui, Z. Zeng, B. Liang, W. Chen, M. Liu, Y. Zhu, A. Cao, Z. Tang, Biomimetic carbon nanotube films with gradient structure and locally tunable mechanical property, *Adv. Funct. Mater.* 25 (2015) 7173–7179, <https://doi.org/10.1002/adfm.201503341>.
- [27] O. Zvarec, S. Purushotham, A. Masic, R.V. Ramanujan, A. Miserez, Catechol-functionalized chitosan/iron oxide nanoparticle composite inspired by mussel thread coating and squid beak interfacial chemistry, *Langmuir* 29 (2013) 10899–10906, <https://doi.org/10.1021/la401858s>.
- [28] X. Zhang, P. Hassanzadeh, T. Miyake, J. Jin, M. Rolandi, Squid beak inspired water processable chitosan composites with tunable mechanical properties, *J. Mater. Chem. B* 4 (2016) 2273–2279, <https://doi.org/10.1039/C6TB00106H>.
- [29] J.A. Neal, N.J. Oldenhuis, A.L. Novitsky, E.M. Samson, W.J. Thrift, R. Ragan, Z. Guan, Large continuous mechanical gradient formation via metal-ligand interactions, *Angew. Chem. Int. Ed.* 56 (2017) 15575–15579, <https://doi.org/10.1002/anie.201707587>.
- [30] L. Hsu, C. Weder, S.J. Rowan, Stimuli-responsive, mechanically-adaptive polymer nanocomposites, *J. Mater. Chem.* 21 (2011) 2812–2822, <https://doi.org/10.1039/C0JM02383C>.
- [31] J.R. Capadona, K. Shanmuganathan, D.J. Tyler, S.J. Rowan, C. Weder, Stimuli-responsive polymer nanocomposites inspired by the sea cucumber dermis, *Science* 319 (2008) 1370–1374, <https://doi.org/10.1126/science.1153307>.
- [32] K. Shanmuganathan, J.R. Capadona, S.J. Rowan, C. Weder, Bio-inspired mechanically-adaptive nanocomposites derived from cotton cellulose whiskers, *J. Mater. Chem.* 20 (2009) 180–186, <https://doi.org/10.1039/B916130A>.
- [33] K. Shanmuganathan, J.R. Capadona, S.J. Rowan, C. Weder, Stimuli-responsive mechanically adaptive polymer nanocomposites, *ACS Appl. Mater. Interfaces* 2 (2010) 165–174, <https://doi.org/10.1021/am9006337>.
- [34] K.L. Dagnon, K. Shanmuganathan, C. Weder, S.J. Rowan, Water-triggered modulus changes of cellulose nanofiber nanocomposites with hydrophobic polymer matrices, *Macromolecules* 45 (2012) 4707–4715, <https://doi.org/10.1021/ma300463y>.
- [35] J. Mendez, P.K. Annamalai, S.J. Eichhorn, R. Rusli, S.J. Rowan, E.J. Foster, C. Weder, Bioinspired mechanically adaptive polymer nanocomposites with water-activated shape-memory effect, *Macromolecules* 44 (2011) 6827–6835, <https://doi.org/10.1021/ma201502k>.
- [36] J.R. Capadona, K. Shanmuganathan, S. Trittschuh, S. Seidel, S.J. Rowan, C. Weder, Polymer nanocomposites with nanowhiskers isolated from microcrystalline cellulose, *Biomacromolecules* 10 (2009) 712–716, <https://doi.org/10.1021/bm8010903>.
- [37] R.J. Moon, A. Martini, J. Nairn, J. Simonsen, J. Youngblood, Cellulose nanomaterials review: structure, properties and nanocomposites, *Chem. Soc. Rev.* 40 (2011) 3941–3994, <https://doi.org/10.1039/C0CS00108B>.
- [38] S.J. Eichhorn, A. Dufresne, M. Aranguren, N.E. Marcovich, J.R. Capadona, S.J. Rowan, C. Weder, W. Thielemans, M. Roman, S. Renneckar, W. Gindl, S. Veigel, J. Keckes, H. Yano, K. Abe, M. Nogi, A.N. Nakagaito, A. Mangalam, J. Simonsen, A.S. Benight, A. Bismarck, L.A. Berglund, T. Peijs, Review: current international research into cellulose nanofibres and nanocomposites, *J. Mater. Sci.* 45 (2009) 1, <https://doi.org/10.1007/s10853-009-3874-0>.
- [39] Y. Habibi, L.A. Lucia, O.J. Rojas, Cellulose nanocrystals: chemistry, self-assembly, and applications, *Chem. Rev.* 110 (2010) 3479–3500, <https://doi.org/10.1021/cr900339w>.
- [40] S.J. Eichhorn, Stiff as a board: perspectives on the crystalline modulus of cellulose, *ACS Macro Lett.* 1 (2012) 1237–1239, <https://doi.org/10.1021/mz300420k>.
- [41] P. Tingaut, T. Zimmermann, G. Sèbe, Cellulose nanocrystals and microfibrillated cellulose as building blocks for the design of hierarchical functional materials, *J. Mater. Chem.* 22 (2012) 20105–20111, <https://doi.org/10.1039/C2JM32956E>.
- [42] R. Rusli, K. Shanmuganathan, S.J. Rowan, C. Weder, S.J. Eichhorn, Stress transfer in cellulose nanowhisker composites—Influence of whisker aspect ratio and surface charge, *Biomacromolecules* 12 (2011) 1363–1369, <https://doi.org/10.1021/bm200141x>.
- [43] S. Eyley, W. Thielemans, Surface modification of cellulose nanocrystals, *Nanoscale* 6 (2014) 7764–7779, <https://doi.org/10.1039/C4NR01756K>.
- [44] N. Lin, J. Huang, A. Dufresne, Preparation, properties and applications of polysaccharide nanocrystals in advanced functional nanomaterials: a review, *Nanoscale* 4 (2012) 3274–3294, <https://doi.org/10.1039/C2NR30260H>.
- [45] S. Wohlhauser, G. Delepierre, M. Labet, G. Morandi, W. Thielemans, C. Weder, J.O. Zoppe, Grafting polymers from cellulose nanocrystals: synthesis, properties, and applications, *Macromolecules* 51 (2018) 6157–6189, <https://doi.org/10.1021/acs.macromol.8b00733>.
- [46] S.A. Kedzior, M. Kiriakou, E. Niinivaara, M.A. Dubé, C. Fraschini, R.M. Berry, E.D. Cranston, Incorporating cellulose nanocrystals into the core of polymer latex particles via polymer grafting, *ACS Macro Lett.* 7 (2018) 990–996, <https://doi.org/10.1021/acsmacrolett.8b00334>.
- [47] J.-M. Malho, J. Brand, G. Pecastaings, J. Ruokolainen, A. Gröschel, G. Sèbe, E. Garanger, S. Lecommandoux, Multifunctional stimuli-responsive cellulose nanocrystals via dual surface modification with genetically engineered elastin-like polypeptides and poly(acrylic acid), *ACS Macro Lett.* 7 (2018) 646–650, <https://doi.org/10.1021/acsmacrolett.8b00321>.
- [48] Z. Wang, Y. Zhang, L. Yuan, J. Hayat, N.M. Trenor, M.E. Lamm, L. Vlaminc, S. Billiet, F.E. Du Prez, Z. Wang, C. Tang, Biomass approach toward robust sustainable, multiple-shape-memory materials, *ACS Macro Lett.* 5 (2016) 602–606, <https://doi.org/10.1021/acsmacrolett.6b00243>.
- [49] Y. Zhang, V. Karimkhani, B.T. Makowski, G. Samaranyake, S.J. Rowan, Nanoemulsions and nanolatexes stabilized by hydrophobically functionalized cellulose nanocrystals, *Macromolecules* 50 (2017) 6032–6042, <https://doi.org/10.1021/acs.macromol.7b00982>.
- [50] A.E. Way, L. Hsu, K. Shanmuganathan, C. Weder, S.J. Rowan, pH-responsive cellulose nanocrystal gels and nanocomposites, *ACS Macro Lett.* 1 (2012) 1001–1006, <https://doi.org/10.1021/mz3003006>.
- [51] E. Cudjoe, S. Khani, A.E. Way, M.J.A. Hore, J. Maia, S.J. Rowan, Biomimetic reversible heat-stiffening polymer nanocomposites, *ACS Cent. Sci.* 3 (2017) 886–894, <https://doi.org/10.1021/acscentsci.7b00215>.
- [52] M.V. Biyani, C. Weder, E. Johan Foster, Photoswitchable nanocomposites made from coumarin-functionalized cellulose nanocrystals, *Polym. Chem.* 5 (2014) 5501–5508, <https://doi.org/10.1039/C4PY00486H>.
- [53] M.V. Biyani, M. Jorfi, C. Weder, E. Johan Foster, Light-stimulated mechanically switchable, photopatternable cellulose nanocomposites, *Polym. Chem.* 5 (2014) 5716–5724, <https://doi.org/10.1039/C4PY00487F>.
- [54] K. Song, H. Xu, K. Xie, Y. Yang, Keratin-based biocomposites reinforced and cross-linked with dual-functional cellulose nanocrystals, *ACS Sustain. Chem. Eng.* 5 (2017) 5669–5678, <https://doi.org/10.1021/acssuschemeng.7b00085>.
- [55] R. Dash, M. Foston, A.J. Ragauskas, Improving the mechanical and thermal properties of gelatin hydrogels cross-linked by cellulose nanowhiskers, *Carbohydr. Polym.* 91 (2013) 638–645, <https://doi.org/10.1016/j.carbpol.2012.08.080>.
- [56] N.M. Girouard, S. Xu, G.T. Schueneman, M.L. Shofner, J.C. Meredith, Site-selective modification of cellulose nanocrystals with isophorone diisocyanate and formation of polyurethane-CNC composites, *ACS Appl. Mater. Interfaces* 8 (2016) 1458–1467, <https://doi.org/10.1021/acsmi.5b10723>.
- [57] C. Shao, M. Wang, H. Chang, F. Xu, J. Yang, A self-healing cellulose nanocrystal-poly(ethylene glycol) nanocomposite hydrogel via Diels-Alder Click Reaction, *ACS Sustain. Chem. Eng.* 5 (2017) 6167–6174, <https://doi.org/10.1021/acssuschemeng.7b01060>.
- [58] J. Yang, C.-R. Han, X.-M. Zhang, F. Xu, R.-C. Sun, Cellulose nanocrystals mechanical reinforcement in composite hydrogels with multiple cross-links: correlations between dissipation properties and deformation mechanisms, *Macromolecules* 47 (2014) 4077–4086, <https://doi.org/10.1021/ma500729q>.
- [59] J.D. Fox, J.R. Capadona, P.D. Marasco, S.J. Rowan, Bioinspired water-enhanced mechanical gradient nanocomposite films that mimic the architecture and properties of the squid beak, *J. Am. Chem. Soc.* 135 (2013) 5167–5174, <https://doi.org/10.1021/ja4002713>.
- [60] K.L. Dagnon, A.E. Way, S.O. Carson, J. Silva, J. Maia, S.J. Rowan, Controlling the rate of water-induced switching in mechanically dynamic cellulose nanocrystal composites, *Macromolecules* 46 (2013) 8203–8212, <https://doi.org/10.1021/ma4008187>.
- [61] N. Lin, A. Dufresne, Physical and/or chemical compatibilization of extruded cellulose nanocrystal reinforced polystyrene nanocomposites, *Macromolecules* 46 (2013) 5570–5583, <https://doi.org/10.1021/ma4010154>.
- [62] P.K. Annamalai, K.L. Dagnon, S. Monemian, E.J. Foster, S.J. Rowan, C. Weder, Water-responsive mechanically adaptive nanocomposites based on styrene-butadiene rubber and cellulose nanocrystals—processing matters, *ACS Appl. Mater. Interfaces* 6 (2014) 967–976, <https://doi.org/10.1021/am404382x>.